Applied Surface Science 573 (2022) 151584

Contents lists available at ScienceDirect

Applied Surface Science

journal homepage: www.elsevier.com/locate/apsusc

Full Length Article

Dependence of cationic dyes' adsorption upon α-MoO_3 structural properties

Endre-Zsolt Kedves [a,b,c], Enikő Bárdos [d], Tamás Gyulavári [d], Zsolt Pap [b,d,e,*], Klara Hernadi [d,f], Lucian Baia [a,b,e,*]

[a] Faculty of Physics, Babeş-Bolyai University, M. Kogălniceanu 1, Cluj-Napoca RO-400084, Romania
[b] Centre of Nanostructured Materials and Bio-Nano Interfaces, Institute for Interdisciplinary Research on Bio-Nano-Sciences, Treboniu Laurian 42, Cluj-Napoca RO-400271, Romania
[c] Department of Biosystems Engineering, Faculty of Engineering, University of Szeged, Moszkvai krt. 9, H-6725 Szeged, Hungary
[d] Department of Applied and Environmental Chemistry, University of Szeged, Rerrich tér 1, HU-6720 Szeged, Hungary
[e] Laboratory for Advanced Materials and Applied Technologies, Institute for Research, Development and Innovation in Applied Natural Sciences, Fantanele 30, Cluj-Napoca RO-400294, Romania
[f] Institute of Physical Metallurgy, Metal Forming and Nanotechnology, University of Miskolc, HU-3515 Miskolc-Egyetemváros, Hungary

ARTICLE INFO

Keywords:
α-MoO_3
Adsorption
Cationic dyes
Photocatalytic activity
Inhibition

ABSTRACT

Orthorhombic molybdenum oxide (α-MoO_3) samples were prepared via calcination. During this process, the ratio of the (040)/(110) or (040)/(021) crystallographic planes was fine-tuned by applying different calcination temperatures. Textural characterization of the samples was carried out to comprehend their differences in photocatalytic and adsorption applications. Except for methyl orange, all the tested dyes (methylene blue, crystal violet, malachite green, and rhodamine B) presented adsorption affinity towards α-MoO_3. It was revealed that the presence of α-MoO_3 significantly decreased the photocatalytic performance of TiO_2 under UV light irradiation. With the growth of the (040) facet of α-MoO_3, the photocatalytic activity increased while the adsorption affinity decreased for cationic dyes. It was found that the solubility of α-MoO_3 depends on the proportional presence of the (040) facet, which determines both the adsorption and photocatalytic behaviors of the oxide. The solubility of α-MoO_3 is reflected by the decreasing rate of solution pH, hence the adsorption can be measured accurately, but it varies according to the cationic dye structure. Using cationic dyes to assess the photocatalytic activity of α-MoO_3 requires meticulous investigations since adsorption can be mistaken with photocatalytic activity: the adsorption rate depends on both adsorptive and adsorbent structures.

1. Introduction

Differently shaped metal oxide nanoparticles have received increased attention, due to their potential applicability in the field of advanced oxidation processes [1–5], especially in the field of photocatalysis. Besides the well-known TiO_2, the list of efficient photocatalysts is continuously extending and further investigations have been carried out regarding their crystalline structure to understand and enhance the catalytic process. The main interests are: improving the quantum efficiency, lowering the excitation energy from UV to visible light (because visible light is a large part of the solar spectrum [6]), and reducing the photoexcited electron–hole pair recombination rate. Concerning the enhancement of visible light response of semiconductors, different strategies have been reported:, doping with transition metal ions [7–9], coupling various semiconductors [10,11], and putting emphasis on researching various oxides that inherently possess relatively low band gap energy.

Molybdenum trioxide (MoO_3), has a relatively wide band gap of 2.6–3.6 eV which makes it an excellent candidate in visible-light-driven photocatalytic processes [12]. The applicability of MoO_3 is becoming more widespread due to its unique structural and optical properties: as photo- and electrochromic devices, photo- and electrocatalytic devices (hydrogen evolution), and as battery systems [13–15]. MoO_3 has three crystal phases: orthorhombic (α-MoO_3), hexagonal (h-MoO_3) and monoclinic (β-MoO_3). From a morphological aspect, it appears mainly in fibrous form, but the morphology can vary from nanotubes to hexagons or even from nanosheets to nanoplates [16–18]. A conspicuous feature of α-MoO_3 is the fibrous morphology due to its anisotropic layered

* Corresponding authors at: Centre of Nanostructured Materials and Bio-Nano Interfaces, Institute for Interdisciplinary Research on Bio-Nano-Sciences, Treboniu Laurian 42, Cluj-Napoca RO-400271, Romania. Department of Applied and Environmental Chemistry, University of Szeged, Rerrich tér 1, HU-6720 Szeged, Hungary.
E-mail addresses: pzsolt@chem.u-szeged.hu (Z. Pap), lucian.baia@ubbcluj.ro (L. Baia).

https://doi.org/10.1016/j.apsusc.2021.151584
Received 8 July 2021; Received in revised form 22 September 2021; Accepted 9 October 2021
Available online 12 October 2021

crystalline structure formed by van der Waals interactions along the [0 1 0] direction by stacking MoO_6 octahedrons [19]. Many papers have presented various synthesis routes to influence the morphology of MoO_3 nanostructures, such as thermal evaporation, chemical vapor deposition, and the well-known solvothermal method [20–22].

Among the three types of crystal structure, the thermodynamically stable orthorhombic structure has received special attention, both by itself and in composites (with TiO_2, MoS_2, WO_3, graphene, Ag, Bi_2O_3, ZnO) [23–28], in the field of photocatalysis, adsorption, and gas-sensing [29–32]. Interestingly, α-MoO_3 in photocatalytic processes is more frequently tested with cationic dyes than with other model pollutants, such as methylene blue, rhodamine B [29,33–37]. Publications concerning effective MoO_3-based catalysts for the degradation of anionic dyes are scarce [38]. Moreover, the photocatalytic reduction of Cr(VI) with MoO_3 is often discussed, which increases the publication frequency in the field of photocatalysis and covers a significant part of the papers containing the "MoO_3 photocat*" keywords [39–41].

Based on data collected from the Web of Science, MoO_3 is increasingly investigated in the field of photocatalysis but the number of publication is still low. Altogether, 165 articles were found using the "MoO_3 photocat*" search terms, of which 121 papers were published between 2015 and 2020 (Fig. 1). On the other hand, the adsorption properties of MoO_3 are less studied, as we found only 71 papers, containing "MoO_3 ads*" in the title, from which 29 papers were published since 2015 (Fig. 1).

Recently, α-MoO_3 has been recognised as an effective adsorbent using rhodamine B and methylene blue as adsorptives, but the emphasis was put mainly on the adsorbents' performance. At the same time, scant attention has been paid to the correlation of the structural features of α-MoO_3 and the adsorption mechanism of different cationic dyes.

Hereby, α-MoO_3 samples were prepared with different structure to examine their dye-removal efficiency from aqueous solutions in the light of the detailed structural properties of oxide, from the perspective of both photocatalytic (in composite with TiO_2) and adsorption processes. We observed no enhancement but inhibition during photocatalytic tests, meanwhile, the adsorption capacity of α-MoO_3 was prominent for cationic dyes. We noticed that in an aqueous medium α-MoO_3 powder causes acidification, which depends on the crystalline (0 4 0)/(0 2 1) or (0 4 0)/(1 1 0) facet ratios, and can be correlated to the adsorption degree.

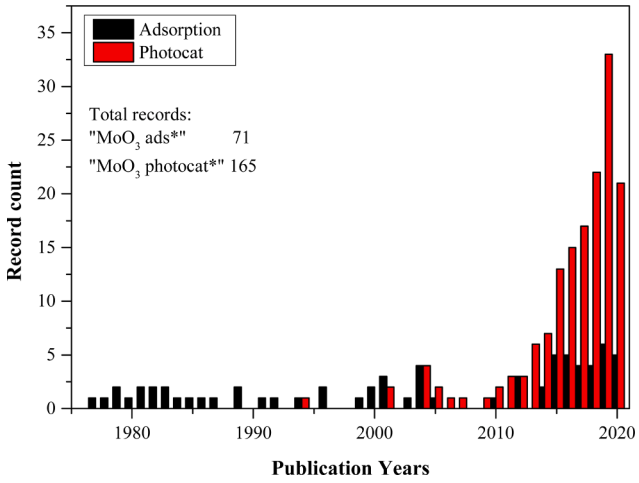

Fig. 1. Published articles before 2021 containing "MoO_3 ads*" and "MoO_3 photocat*" in their titles, according to Web of Scince (at 04.02.2021).

2. Experimental section

2.1. Preparation of α-MoO_3 with different crystal facet ratio

2 g of commercial α-MoO_3 (Alfa Aesar, Molybdenum(VI) oxide, 99.5%) powder was annealed for 2 h at 500, 600, 650, 700 and 750 °C – therefore the samples were called as follows: "α-MoO_3" following by a number which indicates the calcination temperature. The commercial α-MoO_3 powder kept its slightly grey color below 650 °C. After reaching 650 °C, the powder's color turned yellow. After the heat treatment, all samples were pulverized in an agate mortar. For photocatalytic investigations, 1.8 g of TiO_2 (Evonik Industries P25) and 0.2 g MoO_3 sample were prepared in an agate mortar (90/10 wt%).

2.2. Characterization methods

X-ray diffraction (XRD) measurements were performed on a Rigaku Miniflex-II diffractometer using characteristic CuK_α X-ray radiation (2θ° = 5–80°, 20°·min^{-1}, λ = 0.15418 nm).

A JASCO-V650 spectrophotometer with an integration sphere (ILV-724) was used to measure the diffuse reflectance spectra of the composite samples (λ = 250–800 nm). $BaSO_4$ was used as a reference. The indirect band gap of the TiO_2/MoO_3 composites was determined via the Kubelka–Munk method (Fig. S1)[42].

Raman measurements were carried out with a Thermo Scientific DXR Raman microscope, equipped with a diode-pumped frequency-doubled Nd:YAG laser with 10 mW maximum power. The sample was irradiated by a laser with a wavelength of 532.2 nm and the measurements were performed with a spectral resolution of 4 cm^{-1}. An area of 5 × 5 μm was used for data acquisition.

The Fourier-transform infrared spectroscopy (FT-IR) data was used to obtain FT-IR absorption spectra (JASCO 4100 spectrometer), in the range of 400–4000 cm^{-1}, with 4 cm^{-1} spectral resolution using KBr pellets as a reference. The pellets were prepared by mixing 1.0–1.2 mg of MoO_3 and 200 mg of KBr.

The microcrystalline structure of the samples was analyzed by field emission scanning electron microscopy (SEM), Hitachi S-4700 Type II FE-SEM operated at 10 kV. The samples were attached to a carbon adhesive tape which was fixed on an aluminum sample holder.

A FEI Technai G2 X-TWIN TEM (200 kV) transmission electron microscope was used to take micrographs about the morphology of the particles. The samples were prepared as follows: a small amount of the examined materials was suspended in 1.25 cm^3 of ethanol. A few drops from this suspension were deposited and dried onto the surface of a CF 200 Cu TEM grid.

α-MoO_3 samples' zeta potential (ζ-potential) was measured three times using a using a dynamic light scattering analyzer (Nano ZS90 Zetasizer, Malvern Instruments equipped with a He–Ne laser (633 nm, 5 mW)) and the mean value with its corresponding standard deviation has been reported.

During the adsorption and photocatalytic investigations, the quantitative analysis of the dyes was carried out using an Analytic Jena Specord 250 plus UV–Vis spectrophotometer. During the latter, the dyes' spectra were recorded in the range of 250–650 nm for each sample. As a reference, the photocatalytic activity of P25 was also measured.

The photocatalytic reactor was made of pyrex glass with a cooling jacket, surrounded by 6 × 6 W fluorescent lamps, ($\lambda_{max} \approx 360$ nm). The volume of MO solution was $V_{MO} = 120$ mL, with an initial concentration of $c_0 = 125$ μM, and the suspension concentration was $c_{catalyst} = 1$ g·L^{-1}. The solution was mixed at 500 rpm, irradiated for 2 h, and the temperature was maintained at 25 °C by recirculating water. We took 1.5 mL of samples during the photocatalytic experiments.

To obtain adsorption isotherms, 50 mL of the dye solution with a concentration of 50 μM was prepared with various adsorbent amounts (0.01–1.00 g·L^{-1}). The suspension was kept for 20 h in the dark, without mechanical mixing, at room temperature to reach adsorption/

desorption equilibrium. Henceforward, we measured the solution pH with a SenTix@980 pH electrode, and took 1.5 mL aliquots from each solution, and recorded their absorption spectra. The gathered samples were separated by a Whatman microfilter containing an inorganic membrane with a 0.02 μm pore diameter. The samples were not centrifuged because of the possible temperature fluctuations that may occur during this process, influencing the adsorption process significantly. The pH of the suspension was also followed for 30 min for each α-MoO_3 sample to investigate the correlation between the adsorption rate and the pH change of the solution.

Methyl orange (MO) was used for the photocatalytic tests, while the cationic dyes such as rhodamine B (RhB), methylene blue (MB), crystal violet (CV), and malachite green (MG) were used only for the adsorption tests. MO did not show adsorption affinity to α-MoO_3; therefore, just the photocatalytic activity experiments were carried out.

3. Results and discussion

3.1. Structural characterization of α-MoO_3

Our goal was to influence the orthorhombic crystal phase of MoO_3 by tuning its (040) /(021) or (040)/(110) crystallographic plane ratios via changing the annealing temperature. Furthermore, the relationship between the structural changes of α-MoO_3 and its applicative properties (both for adsorption and photodegradation processes) were investigated.

3.2. XRD measurements

The recorded XRD patterns were in good agreement with the reflections of the orthorhombic MoO_3 phase (Card nr. 00–101–1073). The ratio of the (021)/(040) or (110)/(040) crystallographic planes changed with the calcination temperature as expected (Fig. 2). This phenomena was similar to the results obtained by T. H. Chiang and H. C. Yeh. [43], where the preferential growth was observed towards [010]. However, it was observed that the growth of the (040) plane started at 650 °C instead of 600 °C – as it occurs in the above-mentioned reference [43]. Before the annealing process, the average particle size was already around 0.5 μm, therefore it was unreasonable to use the Scherrer equation. Consequently, all size values will be discussed based on different electron microscopy measurements.

To track the orientation changes in the α-MoO_3 samples, three characteristic diffraction peaks were chosen: at 23.5 (110), 25.7 (040), and 27.4 (021) 2θ°. It is worth mentioning that the (021) plane was initially the dominant one, but that changed to the (040) plane as its intensity increased after calcination. This suggests that the crystallization growth occurs in the [010] direction, where the MoO_6 octahedra layers are stacked and held together by van der Waals forces. Considering the intensity ratios between (110) and (040) planes or between (021) and (040) planes (Fig. 2 and Table S1), it can be observed that no significant structural and morphological changes occured below 650 °C. At 650 °C, the (040) plane started to increase and it became the dominant crystallographic plane, also for samples α-MoO_3 700 and 750. Fig. 2 also presents that the orientational analogues of the (040) plane, such as the (020) and (060) planes, increase in intensity together with the intensity of the (040) plane.

3.3. Raman measurements

Fig. 3 illustrates the MoO_3 samples' Raman spectra with the characteristic peaks of orthorhombic MoO_3 [44,45] (supplementary information).

Fig. 3a demonstrates that the heat treatment did not affect the samples' crystal phase. Only a subtle linear change was observed between the two bands in the Raman spectra (260–320 cm^{-1} Fig. 3 b). More precisely, the first band at 282 cm^{-1} increased in intensity relative to the band positioned at 289 cm^{-1}. Both signals were associated with the wagging modes of O═Mo═O describing the local symmetry in α-MoO_3 along the c-axis. Dieterle et al. reported that the ratio of the above-mentioned two bands correlated linearly with the Mo and O stoichiometry of α-MoO_3. This finding provides information about the concentration of oxygen vacancies in the crystal structure [46], hence, the MoO_3 samples' stoichiometry can be assessed using this model. They found that, with the increase of calcination temperature, α-MoO_3 crystals were obtained containing predominantly the (040) crystallographic plane, while based on the Raman spectra (using Dieterle's correlation) the oxygen ratio to Mo increased from 2.945 to 2.955.

Silveira [47] highlighted that the relative intensity of three Raman bands (83–97 cm^{-1}, 116–127 cm^{-1}, and 283–290 cm^{-1}) significantly changed after heat treatment. It must be mentioned that Silveira's results are in contradiction with the empirical relationship proposed by Dieterle [46]. They found that a gradual coalescence occurs in the range of 150–350 °C, evidenced by the SEM micrographs. They also reported that this temperature-dependent data could not be described by the anharmonic decay model of an optical phonon into acoustic phonons [47].

3.4. FT-IR characterization

FT-IR spectra (Fig. 4) were recorded in order to identify the characteristic vibrations of the chemical groups that build up the α-MoO_3 structure and the changes that occur as a result of the applied thermal

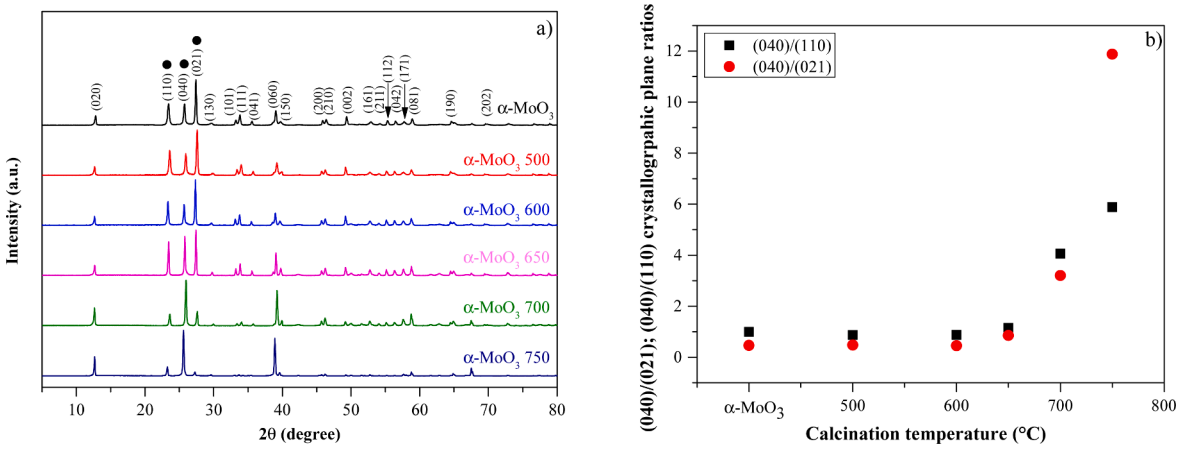

Fig. 2. XRD patterns of orthorhombic (JCPDS Card nr. 00–101–1073) commercial α-MoO_3 and its annealed counterparts (a); Changes in the (040)/(021) and (040)/(110) crystallographic plane ratios as a function of the applied calcination temperature (b).

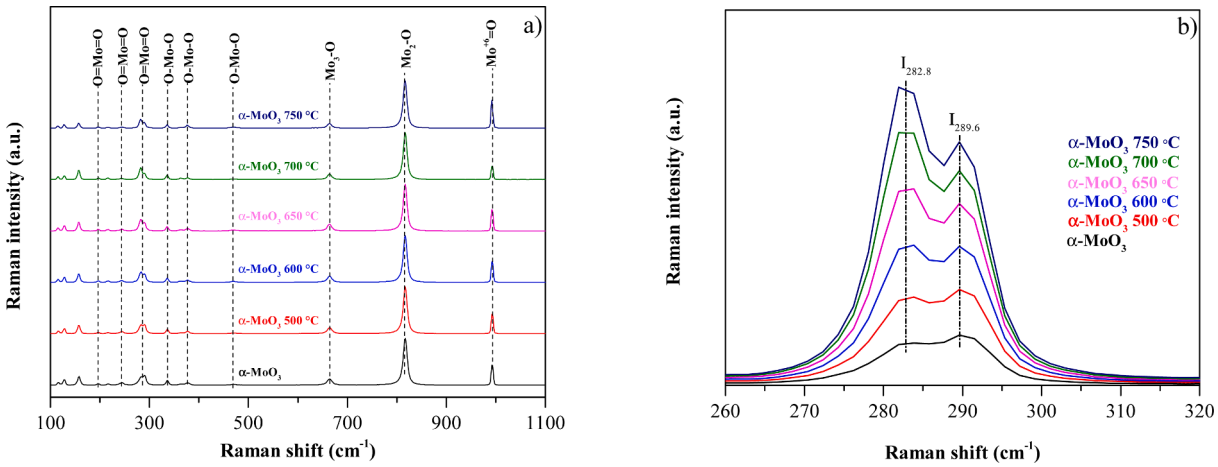

Fig. 3. a) Raman spectra of commercial α-MoO_3 and its annealed counterparts; b) Comparison of the samples' Raman peaks at 282 and 289 cm^{-1}.

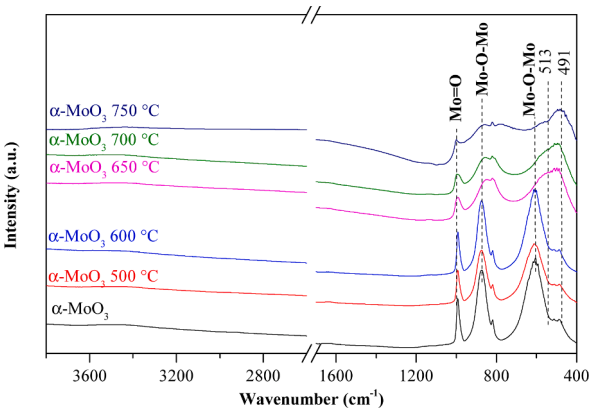

Fig. 4. FT-IR spectra of all α-MoO_3 samples showing a distinct structural change for treatments performed at temperature starting with 650 °C.

treatments. The initial and the heat-treated samples did not contain water-related vibrations (H_2O bending vibrations at 1646 cm^{-1} and the broad absorption band for OH at 3442 cm^{-1}), thus the spectra showed merely the MoO_3 crystal's typical vibrations. Hence, our focus was on the three distinguishable vibrations of α-MoO_3 in the range of 400–1000 cm^{-1} (Fig. 4.) as follows as it is described in supplementary data[18]:

The IR spectra of the samples that were calcined below 600 °C were almost identical. Thereafter, sudden changes occured at 650 °C in the stretching vibrations of Mo and O, but the orthorhombic phase was still present. The signals associated with Mo—O—Mo and Mo_3—O not only widened but also shifted to a higher wavenumber. In addition, α-MoO_3 700 and α-MoO_3 750 showed that the broad absorption band of Mo_3—O continuously shifted towards higher wavenumber values. Thus, one should note that compared to the XRD and Raman results – where a continuous change of the structural characteristics were observed among the investigated samples (Figs. 2 and 3) – the IR spectra (Fig. 4) precisely shows only one sharp structural change for the samples heat treated at temperatures in the range of 600–650 °C.

3.5. Morphological characterization

SEM micrographs of the α-MoO_3 samples are presented in Fig. 5. The micrographs illustrate that morpho-structural changes occured: specifically, the most pronounced changes being related to the shape of the individual crystals and the average particle size. The initial morphology (sample α-MoO_3) could not be stated, as it was irregular. Although by calcination this irregularity was still typical for α-MoO_3 500 and α-MoO_3 600, over 600 °C the morphology changed and platelet-like crystals were obtained. Until the applied heat treatment reached 600 °C the morphology was continuously changing, though the average crystall size was still around 1–2 μm. Following the formation of the platelet-like morphology for α-MoO_3 650 °C, the average crystal size increased to 3–5 μm. Thereafter, the growth process suddenly accelerated, since the average crystal size reached up to 10 μm (α-MoO_3 700) or in some cases even 50 μm (α-MoO_3 750).

The XRD patterns revealed (Fig. 2 a) that the α-MoO_3 crystals evolved in the [0 1 0] direction starting from 650 °C; therefore, the preferred morphology was the platelet-like one. After 650 °C the growth still continued along the [0 1 0] axis. Despite being morphologically identical, α-MoO_3 700 and α-MoO_3 750 showed major differences in the crystallographic plane ratios (XRD patterns), the Mo and O ratio (Raman spectra), and in the Mo_3—O vibrations (IR spectra).

Based on BET measurements the specific surface areas were below the limit of quantification. Considering the relatively large crystal sizes, the specific surface areas were estimated based on the SEM micrographs. With this approach, the α-MoO_3 and α-MoO_3 500 samples were considered as spherical particles while the other samples as cuboids. Our assumption proved to be a good approach because each sample's value was under 5 $m^2 \cdot g^{-1}$. With the increase of average crystal sizes the specific surface areas decreased from 2.12 to 0.18 $m^2 \cdot g^{-1}$ (Table S1).

TEM micrographs confirmed the morphology described above (Fig. 6). As it was expected, irregular and platelet-like crystals were found. The interplanar distance was d = 0.39 nm, which corresponded to the (1 0 0) plane of α-MoO_3, while the (0 0 1) lattice fringes were not visible. The d spacing values were identical for all samples except for α-MoO_3 700 and α-MoO_3 750, in which they could not be determined due to the crystals' thickness. All selected area electron diffraction (SAED) patterns were indexed as the orthorhombic phase of α-MoO_3 using the [0 1 0] zone axis. The SAED patterns were in good agreement with the lattice parameters measured from the high-resolution TEM (HRTEM) micrographs.

3.6. Photocatalytic process

α-MoO_3 samples' photocatalytic performances were assessed in composite with the commercially available TiO_2 P25. Initially, the adsorption of methyl orange (MO) on TiO_2/MoO_3 was excluded by reaching the adsorption/desorption equilibrium in the dark. For this purpose, the suspensions with the model contaminant were stirred for 20 min. Only an insignificant amount of MO was adsorbed on the composite catalysts. Pure P25 almost completely degraded MO (94% conversion) after 2 h.

Despite the composites having similar optical and structural

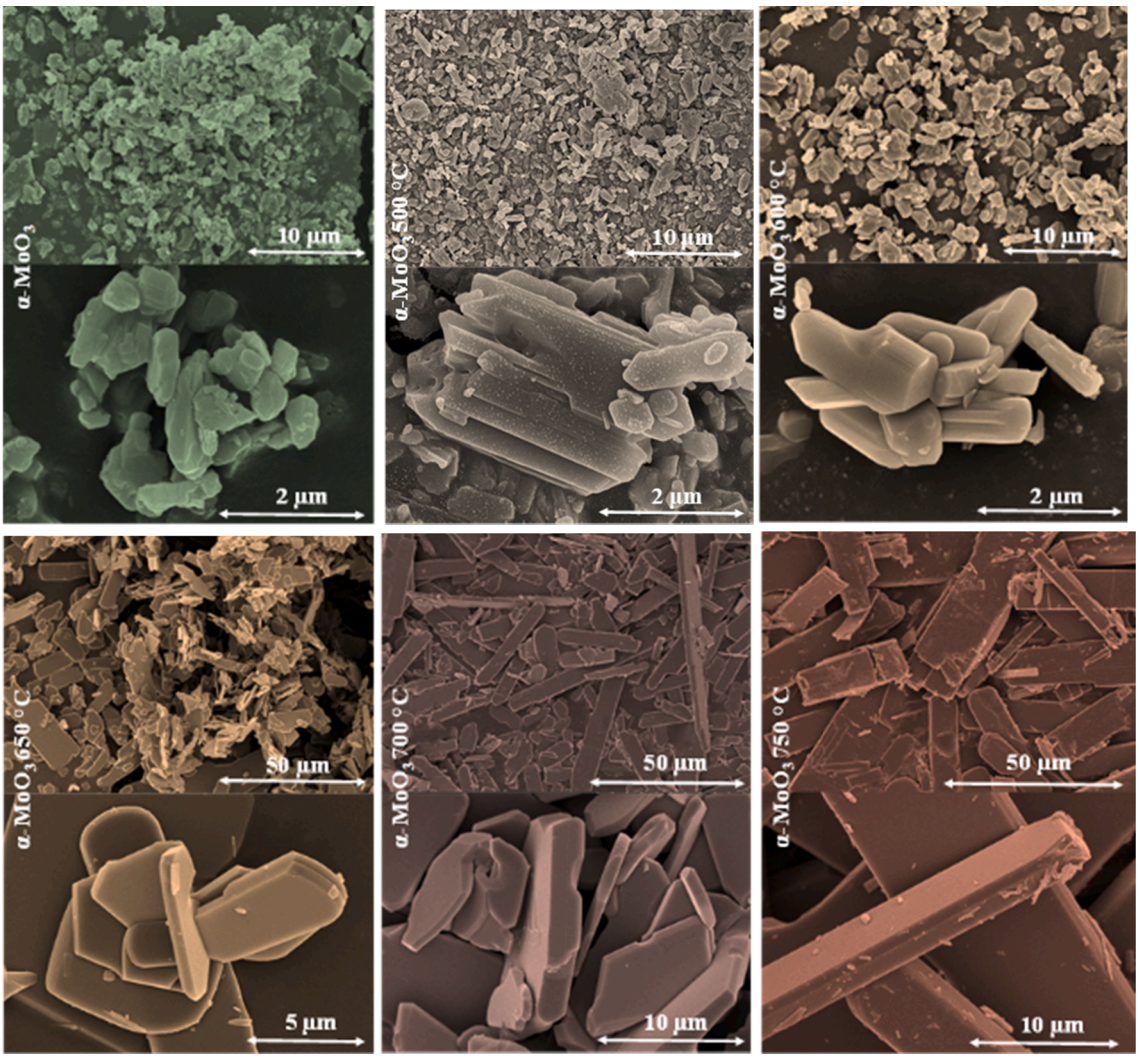

Fig. 5. SEM micrographs of commercial and heat-treated α-MoO_3 samples showing the morphology change from irregular to platelet-like crystals.

properties, the photocatalytic conversion values differed. Unfortunately, each α-MoO_3 sample decreased the photocatalytic activity of P25, however the performance loss decreases with the calcination temperature increment. Among the photocatalytic conversion values, a sudden change was observed after sample α-MoO_3 650 (Fig. 7). α-MoO_3 samples annealed at low temperatures (below <650 °C) highly decreased the photocatalytic activity of TiO_2. The efficiency of P25 was reduced even by ~93.7% (in composite with α-MoO_3 600), which could not have been caused only by the differences in the applied TiO_2 amount. However, a sudden performance enhancement occurred for α-MoO_3 700 and α-MoO_3 750, reaching a conversion of ~49% and ~67%, respectively. Hence, as the applied annealing temperature increased, the degree of photocatalytic inhibition declined. Liu et al. observed that for porous monoliths of α-MoO_3 nanoplates the photocatalytic activity drastically decreased as the thermal treatment temperature increased during methylene blue (MB) degradation [48].

Comparing the MO degradation curves of α-MoO_3 to the P25 reference strongly suggests that the photocatalytic mechanism differs depending on the structure of α-MoO_3. Specifically, in the range of 250–350 nm, an increasing absorbance band was observed (Fig. S2). The presence of this band is proportional to the photocatalytic inhibition, consequently, it can be directly correlated with the with the temperature of the applied heat treatment on α-MoO_3. This signal could be associated with molybdate anion (MoO_4^{-2}), which was generated from molybdic acid (H_2MoO_4) or from the reaction of MoO_3 with hydroxyl groups (OH^-) in aqueous medium [49,50]. The increasing absorption band which implies the molybdate anions are presented in Fig. 7. c. These spectra were calculated by subtracting the MO spectra of a given concentration (different concentration) from the photocatalytically treated absorption spectra of MO Fig. S8.

The formation of MoO_4^{-2} could be affected by different parameters such as temperature, pressure, pH and oxygen fugacity [51]. Therefore, the adsorption and dissociation of water on the surface of α-MoO_3 must influence the photocatalytic performance. With the increase of temperature the intensity of the aforementioned band decreased; consequently, the photocatalytic inhibition of α-MoO_3 declined.

It is known that the pH does not affect the apparent reaction rate of TiO_2 during the degradation of MO in the pH range of 3–5. Moreover, anions can have a quenching effect, as N. Barka also presented that HPO_4^{2-} and CH_3COO^- anions decreased the photocatalytic efficiency of TiO_2 for MO degradation [52]. In another paper, the photocatalytic activity of BiOCl was hindered by other anions, such as HCO_3^-, Cl^-, and NO_3^- [53]. Because the TiO_2 photocatalytic activity is not affected by the pH in the 3–5 interval, we think that essentially molybdate anions presence inhibit the photocatalytic process, so they might have a similar quenching effect as the above-mentioned anions.

Linking the photoactivity of the composites with the structural characteristics of α-MoO_3 showed that the α-MoO_3 samples that contained predominantly the (0 4 0) crystallographic plane exhibited lower inhibition. In addition, the Raman results demonstrated that the ratio of

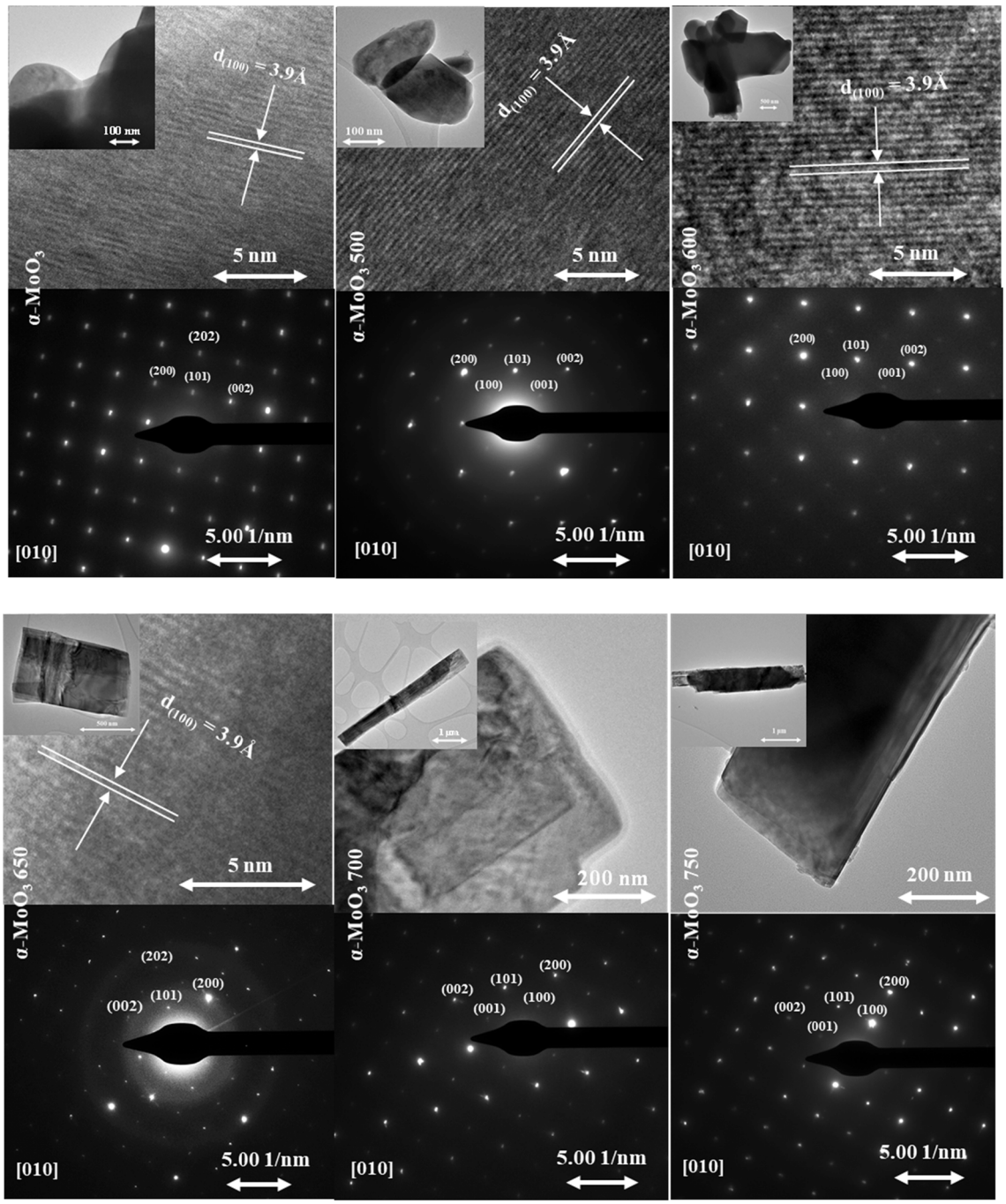

Fig. 6. TEM, HRTEM and SAED micrographs of the MoO_3 samples.

Mo and O increased from 2.945 to 2.955 (based on Dieterle's empirical equation) with the intensity of the (0 4 0) plane. Samples that contained predominantly the (0 4 0) facet showed less solubility in water, which can be evidenced by the absence of the 250–350 nm absorbance band. Our results strongly suggest that the photocatalytic activity of the TiO_2/MoO_3 composites depends on the solubility of α-MoO_3.

Based on the measurements so far it was ascertained that the α-MoO_3 samples showed neither adsorption nor photocatalytic activity using MO as model pollutant. Consequently, their adsorption properties were investigated using cationic dyes, which are the most common model pollutants in the literature to assess the adsorption performance of MoO_3 [35,37,54–56]. For the optimization of adsorbent removal capacity, various isotherm models could be worthwhile to be considered, but such an approach demand preliminary knowledge of the equilibrium characteristics of the removal process for each specific dye. The Langmuir, Freundlich, Temkin, and Dubinin-Radushkevich models and equations are frequently used to describe the equilibrium characteristics of a removal process [57].

The adsorption isotherms were recorded (either for 2 or 20 h) for each dye at a constant dye concentration (50 μM) and by varying the α-MoO_3 amount (Figs. 8 and S3–5). The Langmuir model was the most adequate in the present case, but the adsorption equilibrium could not be determined reliably because the pH was decreasing differently depending on the amount of α-MoO_3. The molybdate ions were also generating during adsorption, as it occurred during photocatalytic experiments the specific band around 250–350 nm (Fig. 8. a, b, d, e blue region) was increasing depending on the α-MoO_3 amount. The most drastic adsorption capacity change occured between the α-MoO_3 600

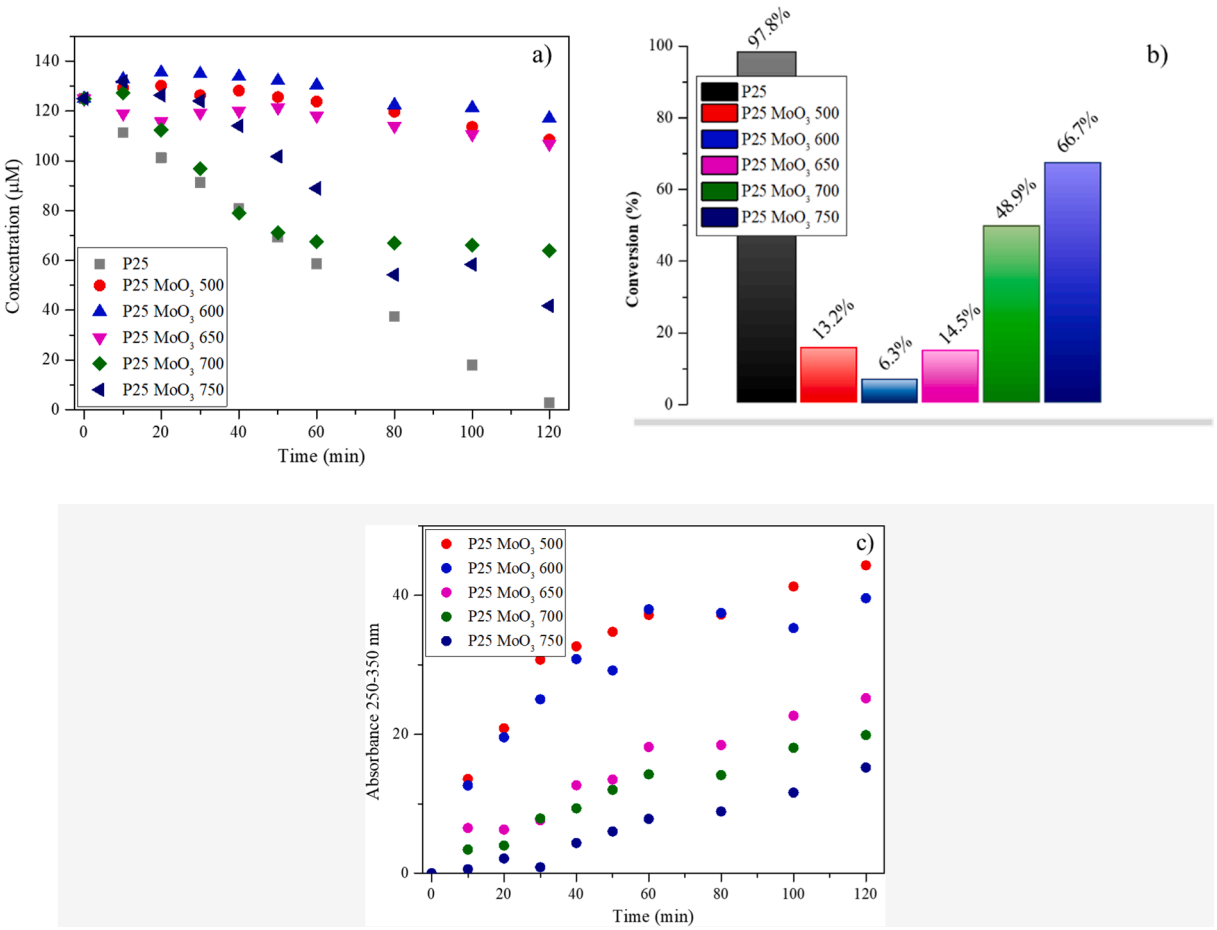

Fig. 7. Photocatalytic degradation of MO with P25 and TiO_2/MoO_3 composites as a function of time a) and the corresponding conversion values b). Peak areas of the 250–350 nm absorbance bands during the photocatalytic degradation of MO with the composites c).

and α-MoO_3 650 samples. The adsorption isotherms of these two samples are shown in Fig. 8 a–f. It was observed that α-MoO_3 600 was a better adsorbent than α-MoO_3 650. α-MoO_3 600 had more advantageous adsorption properties, as for example its surface-normalized adsorption capacity that was found to be higher compared to that of α-MoO_3 650. These clarify that the dyes' adsorption on α-MoO_3 was slightly affected by the specific surface area. Consequently, the surface-area-normalized adsorption values were not identical, implying that other structural characteristics should be responsible for the differences in the samples' adsorption performance. This could originate from the structural properties of the adsorptive, adsorbant or both.

As the amount of H^+ acceptor functional groups decreases, the adsorption capacity of α-MoO_3 also decreased. Crystal violet (CV) has three amine functional groups while malachite green (MG), with a similar structure, has only two. Hence, the cationic dyes' functional groups might have an important role in the adsorption by α-MoO_3. The fast adsorption of MB was favoured due to the presence of two amino, imine, and thiol groups in the molecule. On the other hand, rhodamine B (RhB) has a carboxylic and an ether group besides the two amine groups, which could decrease the adsorption efficiency. The adsorption efficiency decreases based on the number of cationic groups: MB has four, CV has three, MG has two, and RhB also has two, but an ether and a carboxylic group are also present.

The first and the second most sensitive dyes to be adsorbed were CV and MB, respectively. Almost 100% of the dyes were adsorbed after 2 h on 20 mg of α-MoO_3. Both CV and MB presented nearly 100% adsorption after 20 h, even when the adsorbent concentration was 0.1 g·L^{-1} (152.7 mg·g^{-1} for MB, and 199.4 mg·g^{-1} for CV), indicating that the adsorption could progress further. Compared to them, MG and RhB presented lower adsorption affinity (53.05 mg·g^{-1} for RhB and 26.59 mg·g^{-1} for MG) on α-MoO_3. These results strongly suggest that the cationic dyes' functional groups determine the adsorption capacity of α-MoO_3. Santos-Beltrán et al. presented that 400 ppm (~1.25 mM) MB required more than 40 h (2500 min) exposure time to saturate 200 mg·L^{-1} MoO_3 adsorbent [58]. Rakash et al. demonstrated that the adsorption of MB on α-MoO_3 follows the Langmuir model, although other isotherms were also fitted with at least 0.939 R^2. The Langmuir isotherm suggests that MB is adsorbed as a monolayer on α-MoO_3[59]. Their results for MB adsorption presented the best regression correlation coefficient for the pseudo-second-order model: they reached an adsorption capacity of 152 mg·g^{-1} and succeeded to regenerate 99% of the MoO_3 adsorbent by calcination under air atmosphere at 400 °C.

Head et al. presented that water adsorption is strongly disfavored on the MoO_3 (0 1 0) surface, where Mo sites are unreachable [60]. They also proved that only a weak van der Waals interaction occurs between the water H atoms and surface terminal oxygen atoms. However, the adsorption of water molecules can be promoted by species that can interact either with the lone electron pairs on the water O atom, or with unsaturated Mo^{5+} such as surface OH groups. Water dissociation was only favored when water was adsorbed to an unsaturated Mo site through the water's oxygen atom [60]. Our results show indirectly that the unsaturated Mo sites disappeared while the (0 1 0) crystallogpraphic plane increased with the applied heat treatment temperature. So, as the (0 1 0) crystallographic plane developed, the MoO_3 interaction with water should give a declining trend, which is reflected in our photocatalytic experiments by the inhibition efficiency. This suggests that as the adsorption of water is more likely to occur, the photocatalytic performance should deteriorate. On the other hand, the cationic dyes'

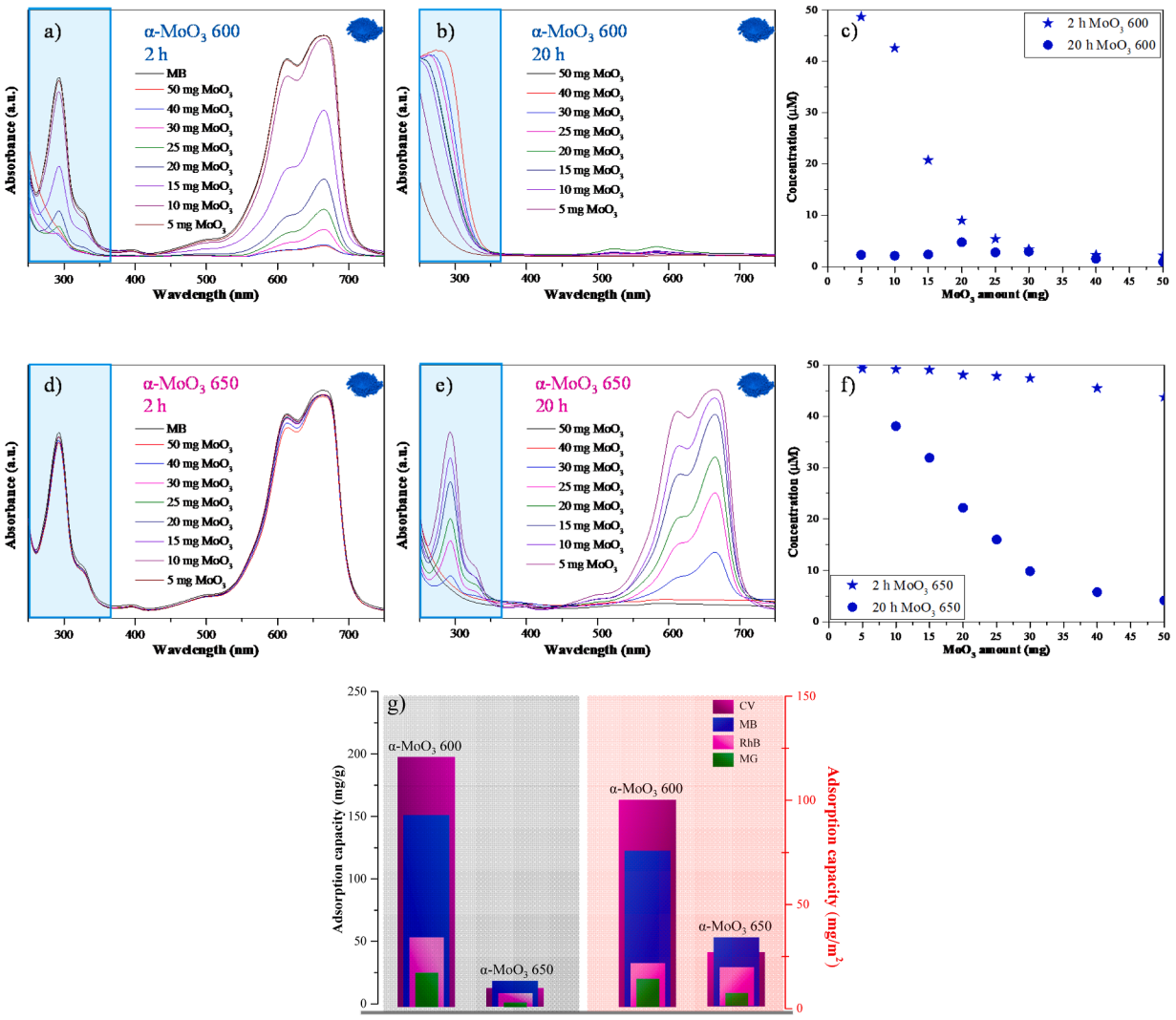

Fig. 8. α-MoO_3 600 (a, b, c) and α-MoO_3 650 (d, e, f) adsorptive's spectra during adsorption and adsorption isotherms of the chosen dye (MB) at 2 h and 20 h. (The other isotherms for α-MoO_3 600 and α-MoO_3 650 for all dyes are presented in Figs. S3-5.); g) adsorption capacity differences after 20 h, for all dyes (comparing the adsorption capcity values mg · g (blue) and mg · m^{-2} (red)) between α-MoO_3 600 and α-MoO_3 650. (For interpretation of the references to colour in this figure legend, the reader is referred to the web version of this article.)

adsorption occurs more likely if water adsorption also takes place. The formation of molybdic acid could cause changes in the pH, which may affect the adsorption process.

3.7. pH measurement experiments

During the adsorption isotherm measurements, it was noticed that the dye solutions' pH decreased to a different degree for every sample. It is known that α-MoO_3 is slightly soluble in water and the following surface reaction may occur:

$$MoO_3 + H_2O \rightleftharpoons HMoO_4^- + H^+ \quad (1)$$

$$HMoO_4^- \rightleftharpoons MoO_4^{2-} + H^+ \quad (2)$$

which can result in the formation of molybdic acid due to the dissociation of $HMoO_4^-$ and MoO_4^{-2} [61]. The van't Hoff isochore equation describes– the temperature dependence of the deprotonation very well. At ambient conditions the acidity constants of molybdic acid are pKa_1 = 3.61–4.0 and pKa_2 = 3.89–4.37[49,62,63]. Moreover, the distribution of three Mo(VI) aqueous species was studied by Z. Minubayeva and T. M. Seward in the 1–9 pH range at different temperatures [63]. The molar absorptivity of the three species are located between 200280 nm, which corresponds with our results from the photocatalytic and adsorption measurements. At 50 °C and pH 7 only MoO_4^{2-} was present, then as the acidity of the solution increased to around pH 6 $HMoO_4^-$ appeared. Finally, around pH 5 H_2MoO_4 started to accumulate [63]. It can be inferred that there is a link between the formed species and the pH of the suspension. Hence, we monitored the pH drop caused by the presence of α-MoO_3 in the four cationic dye solutions (50 μM), and in distilled water as a reference. The pH drop rate strongly depended on the temperature that was applied during the heat treatment of α-MoO_3. Until 600 °C only subtle changes were observed; however, from 650 °C the pH drop rate was significantly lower (Fig. 9). The decrease of pH could be observed in all cases independently of the used dyes. In the first 5 min a sudden pH drop occured, which was followed by a linear pH drop rate. The proton concentration change was the highest during blank experiments (using only water and α-MoO_3). The degree of this decreasing change was gradually lower as the (0 1 0) facet developed. Naturally, the starting pH differed for each dye: for MB and CV it was ≈5.5 pH, while for MG and RhB it was lower than ≈4.5. Interestingly, within a sample the pH drop rate was the same, but the adsorption capacity differed depending on the dye's structure (Fig. 9). This indicated that these dyes had different adsorption rates, although the pH drop rate was the same.

The adsorption capacity of α-MoO_3 for cationic dyes increased with

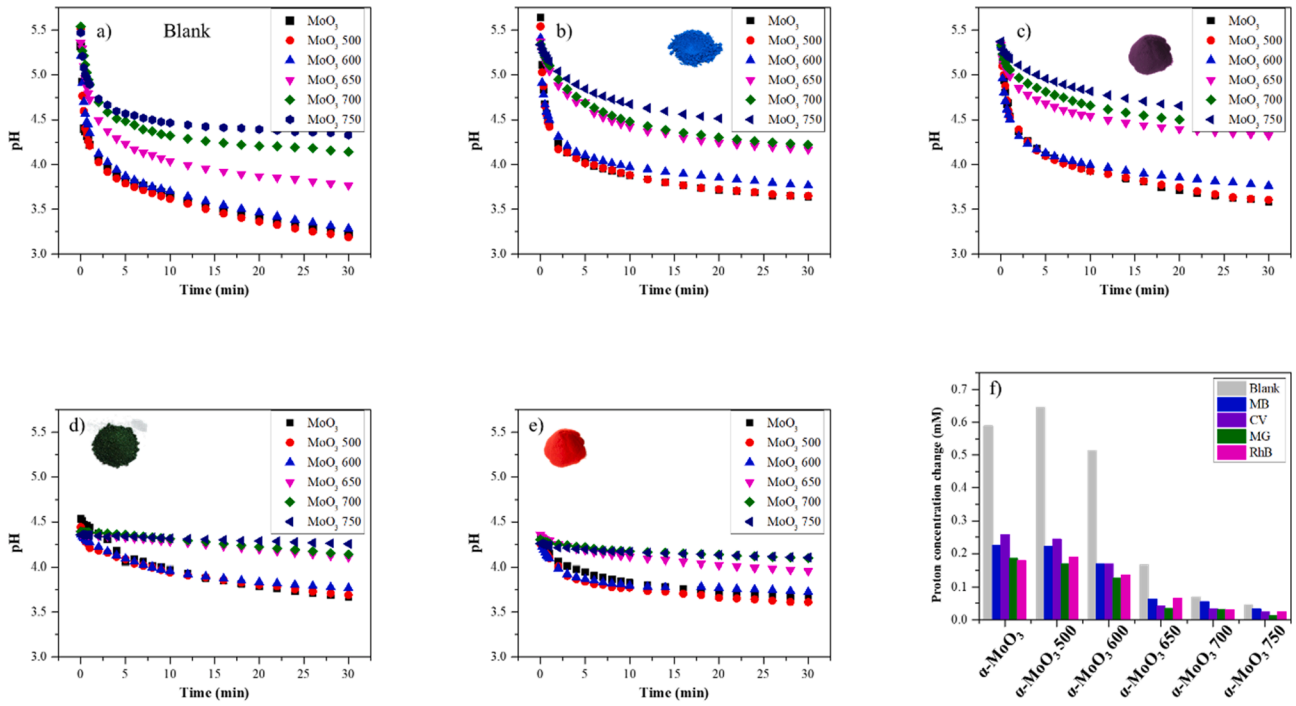

Fig. 9. Observed pH drops in distilled water a) blank, b) MB, c) CV, d) MG, and e) RhB solutions after the addition of the α-MoO_3 samples. The H^+ concentration difference values are presented in the column chart f).

the acidification rate of α-MoO_3. The adsorption capacity and pH drop rate change were highly conspicuous, since the major structural differences appeared between the α-MoO_3 600 and α-MoO_3 650 samples. Conversely, MoO_3 700 and MoO_3 750, with the lowest adsorption capacity, caused the lowest inhibition during the photocatalytic degradation of MO (an anionic dye, which did not adsorb on our samples). Yifan Zhang and Soo-Jin Park drew a similar conclusion using MoO_3 nanowire-based mambranes. On these membranes cationic dyes (MB and RhB) adsorbed more likely than MO as an anionic dye [64].

3.8. Role of surface charge during adsorption

If an oxide surface is in contact with water, some of the surface OH groups can behave as Brönsted acids, which very likely happens in MoO_3. If the oxide is negatively or positively charged, it stabilizes the suspension and prevents particle aggregation. On the other hand, depending on the surface charge, anionic and cationic structures tend to attach strongly via electrostatic forces to the surface of the suspended oxide.

We carried out zeta potential measurements to determine the surface charge values of α-MoO_3 individual particles. A good colloidal stability can be achieved for a nanosuspension if the zeta potentials are either below −30 mV or above + 30 mV [65]. In the present case, all of the samples' surface was negatively charged (Fig. 10) and influenced by the calcination temperature. ζ-potential values distinctly describe the nonlinear correlation that exists between the calcination temperature and the surface charge values. Up to the 600 °C calcination temperature only subtle changes occured in the location of the maximum ζ-potential value of the MoO_3 samples, where the ζ-potential values were around –80–90 mV. Afterwards, a faster growth was observed. As expected, having in mind the previously obtained results, starting with the sample MoO_3 650 a sudden increase was noticed in the ζ-potential values from –90.0 to –77.4 mV. Knowing that the adsorptive is a cationic dye, and the pH decreased due to the formation of MoO_4^{2-} (which made the oxide's surface more negatively charged), we assumed that adsorption was a result of an electrostatic interaction.

Adhikaria et al.[66] presented that WO_3 is a promising adsorbent

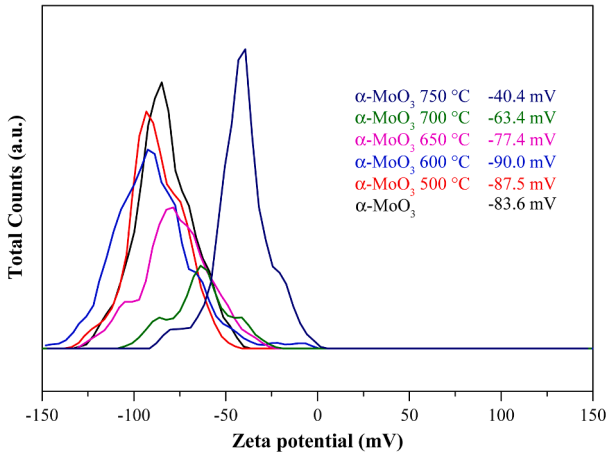

Fig. 10. ζ-potential distribution curves of the MoO_3 samples.

(which follows the Langmuir monolayer adsorption model), to elimintate cationic dyes from aqueous media. They measured –41 mV ζ-potential for WO_3 nanoadsorbent, and reported a similar conclusion that electrostatic attraction can occur very likely between the adsorbent (negatively charged metal oxide) and adsorptive (cationic dye). Moreover it was mentioned that the electrostatic adsorption phenomenon depends on the surface area, heterogeneous adsorption sites, steric hindrance from bulk organic molecules, etc.[66]

In aqueous media the surface properties of α-MoO_3 dynamically changes to achieve its pH_{PCZ} (Fig. 9). This favors the adsorption of cationic dyes; thus, the presence of functional groups such as $–NH_2$ and S^+ might be beneficial. In the present research, the surface charge value defined the adsorption efficiency and capacity. Since the ζ-potential values increased from –83.6 (α-MoO_3) to –40.4 mV (α-MoO_3 750), their pH_{PCZ} values shifted towards a higher pH (which can be affected by the specific surface area and crystal facet ratio). Since the surface chemistry of α-MoO_3 was changed as a result of calcination, the surface

concentration of Brönsted the acid sites must have changed. Our results suggested that the heat treatment deteriorated the OH-rich surface, which could enable the adsorption process. Fig. 9 shows that as the rate of pH change drops, so does the solubility of α-MoO_3 (Equations (1), (2)), which results in a more stable oxide that is ineffective during the adsorption processes.

Besides the ZPT and Raman measurements, the structural characteristics, the adsorption capacities, and the pH drop rates also showed a similar behavior until 600 °C (α-MoO_3 600). Starting with the α-MoO_3 650 sample, not only the adsorption capacity noticeably decreased, but structural changes suddenly occurred as well *(see characterization methods)*.

3.9. Mechanism of cationic dye adsorption

We found that all four cationic dyes had a similar adsorption pattern as a function of pH (Fig. 11). The dyes' structure determined the pH value at which the adsorption process began on α-MoO_3. On the other hand, the acidification rate depended on the α-MoO_3 structure. This confirmed that adsorption occured as a function of α-MoO_3 acidity that is directly related to the crystal structure; more specifically, to the orientation of the crystal. Therefore, the nature of α-MoO_3 established the rate of pH decrease, which directly related to the concentration of the cationic adsorptive. On the other hand, the dye's structure determined the characteristic of the quasi exponential curve and the pH range where the adsorption occurred. The dyes' concentration decreased from 50 to almost 0 μM within different pH intervals (Fig. 11): between 5.5 and 3.7 pH for MB, between 5.2 and 3.8 pH for CV, between 4.5 and 3.3 pH for MG, and between 4.3 and 3.3 pH for RhB. It should be mentioned that this correlation between the pH and the dye concentration is independent of the α-MoO_3 samples' structural properties (Fig. 11). The following exponential equation was used to fit our experimental data (Eq. (3), Table S2):

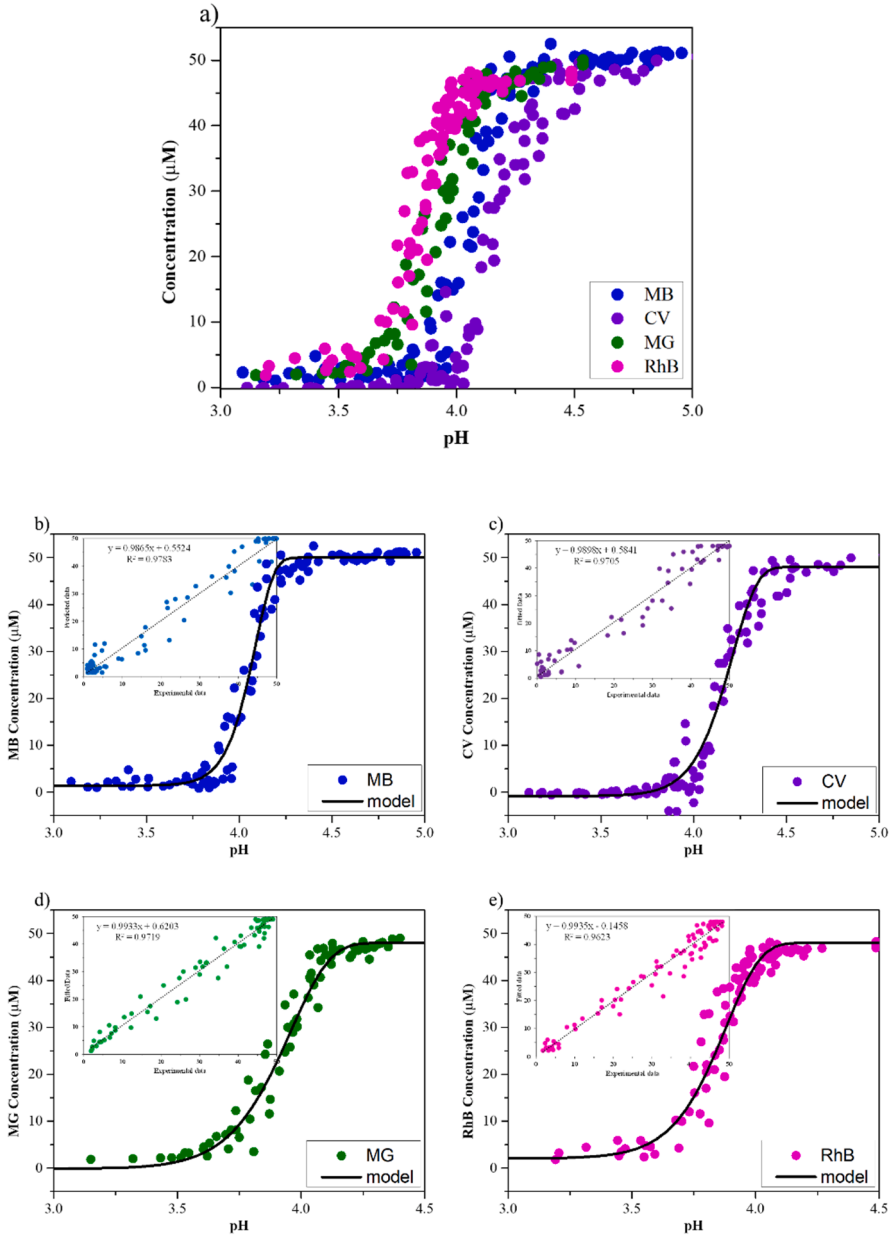

Fig. 11. Dye adsorption curves as a function of pH (a) and correlation of MB (b), CV (c), MG (d), and RhB (e) with pH during the adsorption of α-MoO_3 at 50 μM initial dye concentration.

$$C_{pH} = -\Delta C\hat{A}\cdot e^{-b\hat{A}\cdot(pH_t - pH_{final})^d} + C_0 \quad (3)$$

C_{pH} – colorant's concentration at a given pH [μmol · L^{-1}]
ΔC – C_0–C_{final} [μmol · L^{-1}]
C_0 – colorant's initial concentration [μmol · L^{-1}]
b and d – dye dependent fitted constants
pH_t – pH measured at time t
pH_{final} – the lowest measured pH

The "b" and "d" constans were optimized using the "Fitting Curve" extension of Matlab. The goal was to calculate the dyes' concentration because the sample gathering is very sensitive – most likely the separation of crystals from the liquid sample. Based on this model we calculated the dye's concentration from the pH decay curves to verify the kinetics of the adsorption (Fig. S6).

Based on the pH (Fig. 9 b, c, d, e) decrease and the elaborated empirical model the kinetic constants for both first- and second-order adsorption models were calculated. Our estimation pointed out that the adsorption of MB and CV was at least twice faster than that of MG or RhB (Fig. 11), although the acidification rates were almost the same (Fig. 9). The pseudo-second-order model could be fitted 5 min after the adsorption started, while the pseudo-first-order model covered more data points. The pseudo second-order (plotting $t \cdot q_t^{-1}$ against t) could be spurious, Y. Xiao et al. advise that to verify the assumptions of the model and fit the experimental data with the non linear form of the equation [67]. The residual plot of these data, especially in case of RhB and MG, endorsed that the second order model it might be not valid. Therefore we presume that the obtained adsorption data presents more likely pseudo first-order kinetics for all dyes, however this has to be proven (Fig. S7, Tables S3 and S4).

The preceding data offer prospects in both photocatalytic and adsorption applications. The presented inhibition of the titania's performance is dependent on the structural characteristics of α-MoO_3, but the mechanism is unknown. α-MoO_3 could be a potential scavenger in photocatalytic systems. Even though α-MoO_3 is a well-known visible-light-active photocatalyst, our experiments presented that it could also be a photocatalytic inhibitor. Making composite photocatalysts with MoO_3 could be an effective way to prove the photocatalytic performance excluding other reactions.

Additionally, α-MoO_3 exhibits preferred adsorption depending on the solution's pH. By being aware of the α-MoO_3 characteristics and its pH drop rate, different dyes could be separated by adsorption. Based on our model, for MB adsorption occured below pH ~ 3.9, while for RhB adsorption started at around pH ~ 4.0. Investigating the temperature dependence further could be beneficial to improve this model, which could provide additional data on how the adsorption rate changes.

4. Conclusions

We demonstrated that heat treatment is a feasible way to change α-MoO_3 crystalline facets' ratio. With the growth of the (0 4 0) facet the average crystal size increased, and platelet-like crystals were formed. The broad absorption band of Mo_3–O shifted continuously towards higher energies with the increase of Mo and O ratio. The most recognizable change occurred between the samples that were prepared applying 600 and 650 °C, drastically affecting the applicability of α-MoO_3 in photocatalytic and adsorption processess. Photocatalytic conversion by TiO_2 was highly inhibited in the presence of α-MoO_3, while the cationic dyes' adsorption was enhanced – which worsen as the (0 4 0) facet increased. Based on the literature the (0 4 0) facet does not facilitate water adsorption, which suggests the acidification of the aqueous medium slows down as this facet grows, which was demonstrated by our results. We observed that the structural properties of α-MoO_3 determine mainly the acidification rate, while the dye's structure (depending on the functional groups) establishes the adsorption rate and the pH at which the adsorption starts. Therefore, a strong connection was observed between the acidification of α-MoO_3 suspensions and the cationic dye adsorption, which was described by an empirical equation.

CRediT authorship contribution statement

Endre-Zsolt Kedves: Investigation, Conceptualization, Writing – original draft. **Enikő Bárdos:** Investigation, Conceptualization. **Tamás Gyulavári:** Investigation. **Zsolt Pap:** Supervision, Writing – review & editing. **Klara Hernadi:** Supervision. **Lucian Baia:** Funding acquisition, Supervision, Writing – review & editing.

Declaration of Competing Interest

The authors declare that they have no known competing financial interests or personal relationships that could have appeared to influence the work reported in this paper.

Acknowledgment

Endre-Zsolt Kedves acknowledges the funding provided by the Sapientia Hungariae Foundation, Hungary "Collegium Talentum" scholarship. The authors wish to thank István Székely for the Raman measurements. Zsolt Pap expresses his gratitude towards the Hungarian Academy of Sciences, Bolyai János research scholarship.

Appendix A. Supplementary material

Supplementary data to this article can be found online at https://doi.org/10.1016/j.apsusc.2021.151584.

References

[1] B. Liu, X. Yan, H. Yan, Y. Yao, Y. Cai, J. Wei, S. Chen, X. Xu, L. Li, Materials (Basel) 10 (2017), https://doi.org/10.3390/ma10080976.
[2] S. Sun, T. Deng, H. Ding, Y. Chen, W. Chen, Nanomaterials-Basel 7 (2017), https://doi.org/10.3390/nano7110367.
[3] P. Reñones, A. Moya, F. Fresno, L. Collado, J.J. Vilatela, V.A. de la Peña O'Shea, J. CO2 Util. 15 (2016) 24–31, https://doi.org/10.1016/j.jcou.2016.04.002.
[4] W. Lekphet, T.-C. Ke, C. Su, S. Kathirvel, P. Sireesha, S.B. Akula, W.-R. Li, Appl. Surf. Sci. 382 (2016) 15–26, https://doi.org/10.1016/j.apsusc.2016.04.115.
[5] I. Székely, G. Kovács, L. Baia, V. Danciu, Z. Pap, Materials 9 (2016) 258, https://doi.org/10.3390/ma9040258.
[6] X. Jing, X. Peng, X. Sun, W. Zhou, W. Wang, S. Wang, Mat. Sci. Semicon. Proc. 100 (2019) 262–269, https://doi.org/10.1016/j.mssp.2019.05.004.
[7] R. Alipour Moghadam Esfahani, S.K. Vankova, A.H.A. Monteverde Videla, S. Specchia, Appl. Catal. B-Environ. 201 (2017) 419–429, https://doi.org/10.1016/j.apcatb.2016.08.041.
[8] A. Phuruangrat, U. Cheed-Im, T. Thongtem, S. Thongtem, Mater. Lett. 172 (2016) 166–170, https://doi.org/10.1016/j.matlet.2016.02.141.
[9] M.-V. Sofianou, M. Tassi, V. Psycharis, N. Boukos, S. Thanos, T. Vaimakis, J. Yu, C. Trapalis, Appl Catal B-Envirom 162 (2015) 27–33, https://doi.org/10.1016/j.apcatb.2014.05.049.
[10] H. Salari, M. Kohantorabi, Adv. PowderTechnol. 31 (2020) 493–503, https://doi.org/10.1016/j.apt.2019.11.005.
[11] Y. Zhao, Q. Sun, J. Luo, H. Chen, W. Cai, X. Su, Nano-Struct. Nano-Objects 13 (2018) 93–99, https://doi.org/10.1016/j.nanoso.2017.12.003.
[12] H. Hu, C. Deng, J. Xu, K. Zhang, M. Sun, J. Exp. Nanosci. 10 (2015) 1336–1346, https://doi.org/10.1080/17458080.2015.1012654.
[13] A. Chithambararaj, A.C. Bose, J. Aalloy Compd. 509 (2011) 8105–8110, https://doi.org/10.1016/j.jallcom.2011.05.067.
[14] R.S. Datta, F. Haque, M. Mohiuddin, B.J. Carey, N. Syed, A. Zavabeti, B. Zhang, H. Khan, K.J. Berean, J.Z. Ou, N. Mahmood, T. Daeneke, K. Kalantar-zadeh, J. Mater. Chem. A 5 (2017) 24223–24231, https://doi.org/10.1039/c7ta07705j.
[15] J. Han, X. Ji, X. Ren, G. Cui, L. Li, F. Xie, H. Wang, B. Li, X. Sun, J. Mater. Chem. A 6 (2018) 12974–12977, https://doi.org/10.1039/c8ta03974g.
[16] H.S. Yogananda, H. Nagabhushana, R. Naik, S.C. Prashantha, J. Sci.-Adv. Mater. Dev. 3 (2018) 77–85, https://doi.org/10.1016/j.jsamd.2017.11.001.
[17] T. Nagyne-Kovacs, L. Studnicka, I.E. Lukacs, K. Laszlo, P. Pasierb, I.M. Szilagyi, G. Pokol, Nanomaterials-Basel 10 (2020), https://doi.org/10.3390/nano10050891.
[18] A. Klinbumrung, T. Thongtem, S. Thongtem, J. Nanomater. 2012 (2012) 1–5, https://doi.org/10.1155/2012/930763.
[19] T. Li, W. Zeng, Y. Zhang, S. Hussain, Mater. Lett. 160 (2015) 476–479, https://doi.org/10.1016/j.matlet.2015.08.031.

[20] Y. Li, T. Liu, T. Li, X. Peng, Mater. Lett. 140 (2015) 48–50, https://doi.org/10.1016/j.matlet.2014.10.153.
[21] E. Ghaleghafi, M.B. Rahmani, Solid State Sci. 94 (2019) 85–91, https://doi.org/10.1016/j.solidstatesciences.2019.05.022.
[22] T.N. Kovács, D. Hunyadi, A.L.A. de Lucena, I.M. Szilágyi, J. Therm. Anal. Calorim. 124 (2016) 1013–1021, https://doi.org/10.1007/s10973-015-5201-0.
[23] H. Yu, Y. Li, L. Zhao, G. Li, J. Li, H. Rong, Z. Liu, Mater. Lett. 169 (2016) 65–68, https://doi.org/10.1016/j.matlet.2016.01.097.
[24] J. Li, X. Liu, Mater. Lett. 112 (2013) 39–42, https://doi.org/10.1016/j.matlet.2013.08.094.
[25] T. Liu, B. Li, Y. Hao, Z. Yao, Chem. Eng. J. 244 (2014) 382–390, https://doi.org/10.1016/j.cej.2014.01.070.
[26] H. Liu, T. Lv, C. Zhu, Z. Zhu, Sol. Energ Mat. Sol. C 153 (2016) 1–8, https://doi.org/10.1016/j.solmat.2016.04.013.
[27] L. Cao, Y. Li, J. Wu, W. Li, J. Huang, Y. Feng, C. Yao, J. Li, R. Wang, Q. Kang, L. Feng, J. Aalloy Compd. 744 (2018) 672–678, https://doi.org/10.1016/j.jallcom.2018.02.112.
[28] A. Arfaoui, S. Touihri, A. Mhamdi, A. Labidi, T. Manoubi, Appl. Surf. Sci. 357 (2015) 1089–1096, https://doi.org/10.1016/j.apsusc.2015.09.124.
[29] M. Pérez-González, M. Morales-Luna, J. Santoyo-Salazar, H. Crotte-Ledesma, P. E. García-Tinoco, S.A. Tomás, Catal. Today (2019), https://doi.org/10.1016/j.cattod.2019.06.003.
[30] M.M. Mohamed, T.M. Salama, M. Morsy, R.M.A. Shahba, S.H. Mohamed, Sensor Actuat. B-Chem. 299 (2019), 126960, https://doi.org/10.1016/j.snb.2019.126960.
[31] H.M.M. Munasinghe Arachchige, D. Zappa, N. Poli, N. Gunawardhana, E. Comini, Sensor Actuat. B-Chem. 269 (2018) 331–339, https://doi.org/10.1016/j.snb.2018.04.124.
[32] Y. Yu, W. Zeng, Z. Zhang, Y. Cai, H. Zhang, Mater. Lett. 186 (2017) 119–122, https://doi.org/10.1016/j.matlet.2016.09.106.
[33] A. Chithambararaj, N.S. Sanjini, A.C. Bose, S. Velmathi, Catal. Sci. Technol. 3 (2013) 1405, https://doi.org/10.1039/c3cy20764a.
[34] H. Yang, X. Li, A. Wang, Y. Wang, Y. Chen, Chin. J. Catal. 35 (2014) 140–147, https://doi.org/10.1016/s1872-2067(12)60731-1.
[35] B. Zheng, Z. Wang, X. Wang, Y. Chen, J. Hazard. Mater. 378 (2019), 120753, https://doi.org/10.1016/j.jhazmat.2019.120753.
[36] L. Huang, W. Fang, Y. Yang, J. Wu, H. Yu, X. Dong, T. Wang, Z. Liu, B. Zhao, Mater. Res. Bull. 108 (2018) 38–45, https://doi.org/10.1016/j.materresbull.2018.08.036.
[37] X. Du, X. Wang, Y. Liu, P. Feng, Ceram. Int. 45 (2019) 12599–12601, https://doi.org/10.1016/j.ceramint.2019.03.168.
[38] Y. He, L. Zhang, X. Wang, Y. Wu, H. Lin, L. Zhao, W. Weng, H. Wan, M. Fan, RSC Adv. 4 (2014) 13610–13619, https://doi.org/10.1039/c4ra00693c.
[39] K.S. Al-Namshah, R.M. Mohamed, Ceram. Int. 46 (2020) 6914–6919, https://doi.org/10.1016/j.ceramint.2019.11.187.
[40] Y. Zhang, S.-J. Park, Appl Catal B-Envirom 240 (2019) 92–101, https://doi.org/10.1016/j.apcatb.2018.08.077.
[41] S.L. Prabavathi, P.S. Kumar, K. Saravanakumar, V. Muthuraj, S. Karuthapandian, J. Photochem. Photobiol., A 356 (2018) 642–651, https://doi.org/10.1016/j.jphotochem.2018.02.007.
[42] A.K. Roy Choudhury, 2015, pp. 117–173 https://doi.org/10.1533/9781782423881.117.
[43] T.H. Chiang, H.C. Yeh, Materials (Basel) 6 (2013) 4609–4625, https://doi.org/10.3390/ma6104609.
[44] A. Phuruangrat, S. Thipkonglas, T. Thongtem, S. Thongtem, Mater. Lett. 195 (2017) 37–40, https://doi.org/10.1016/j.matlet.2017.02.053.
[45] M.F.R.C.L. Seguin, J.-C. Lasskgues, Sptxtrochimica Acta Part A 51 (1995) 1323–1344, https://doi.org/10.1016/0584-8539(94)00247-9.
[46] M. Dieterle, G. Weinberg, G. Mestl, PCCP 4 (2002) 812–821, https://doi.org/10.1039/b107012f.
[47] J.V. Silveira, L.L. Vieira, J.M. Filho, A.J.C. Sampaio, O.L. Alves, A.G. Souza Filho, J. Raman Spectrosc. 43 (2012) 1407–1412, https://doi.org/10.1002/jrs.4058.
[48] Y. Liu, P. Feng, Z. Wang, X. Jiao, F. Akhtar, Sci. Rep. 7 (2017) 1845, https://doi.org/10.1038/s41598-017-02025-3.
[49] T.P. Dadze, G.A. Kashirtseva, M.P. Novikov, A.V. Plyasunov, Fluid Phase Equilibr 440 (2017) 64–76, https://doi.org/10.1016/j.fluid.2017.03.003.
[50] J.J. Cruywagen, J.B.B. Heyns, Inorg. Chem. 26 (1987) 2569–2572, https://doi.org/10.1021/ic00263a003.
[51] P. Saha, A.J. Anderson, T. Lee, M. Klemm, Geofluids 2017 (2017) 1–12, https://doi.org/10.1155/2017/5459639.
[52] A.A. Noureddine Barka, Assabbane Nounah, J. Dussaud, Y. Ait Ichou, Phys. Chem. News 41 (85) (2008) 85–88.
[53] D. He, Y. Luo, W. Peng, G. Tang, Q. Guo, X. Gao, J. Water Reuse Desal. 9 (2019) 301–309, https://doi.org/10.2166/wrd.2019.001.
[54] M. Pérez-González, M. Morales-Luna, J. Santoyo-Salazar, H. Crotte-Ledesma, P. E. García-Tinoco, S.A. Tomás, Catal. Today 360 (2021) 138–146, https://doi.org/10.1016/j.cattod.2019.06.003.
[55] A. Chithambararaj, N.S. Sanjini, S. Velmathi, A.C. Bose, PCCP 15 (2013) 14761–14769, https://doi.org/10.1039/c3cp51796a.
[56] Q. Xi, J. Liu, Z. Wu, H. Bi, Z. Li, K. Zhu, J. Zhuang, J. Chen, S. Lu, Y. Huang, G. Qian, Appl. Surf. Sci. 480 (2019) 427–437, https://doi.org/10.1016/j.apsusc.2019.03.009.
[57] N. Ayawei, A.N. Ebelegi, D. Wankasi, J. Chem.-NY 2017 (2017) 1–11, https://doi.org/10.1155/2017/3039817.
[58] A. Santos-Beltrán, M. Santos-Beltrán, F. Paraguay-Delgado, L. Fuentes, R. García, V.G. Orozco, J. Phys. Chem. Solids 121 (2018) 266–275, https://doi.org/10.1016/j.jpcs.2018.05.030.
[59] S. Rakass, H. Oudghiri Hassani, M. Abboudi, F. Kooli, A. Mohmoud, A. Aljuhani, F. Al Wadaani, Molecules 23 (2018), https://doi.org/10.3390/molecules23092295.
[60] A.R. Head, C. Gattinoni, L. Trotochaud, Y. Yu, O. Karslioglu, S. Pletincx, B. Eichhorn, H. Bluhm, J. Phys. Chem. C Nanomater. Interfaces 123 (2019) 16836–16842, https://doi.org/10.1021/acs.jpcc.9b03822.
[61] F.G.-L. Mauricio Escudey, J. Colloid Interf. Sci. 107 (1985) 272–275, https://doi.org/10.1016/0021-9797(85)90173-0.
[62] X. Liu, J. Cheng, M. Sprik, X. Lu, J. Phys. Chem. Lett. 4 (2013) 2926–2930, https://doi.org/10.1021/jz401444m.
[63] Z. Minubayeva, T.M. Seward, Geochim. Cosmochim. AC 74 (2010) 4365–4374, https://doi.org/10.1016/j.gca.2010.04.054.
[64] Y. Zhang, S.J. Park, Micromachines-Basel 10 (2019), https://doi.org/10.3390/mi10090586.
[65] E. Joseph, G. Singhvi (2019) 91–116, https://doi.org/10.1016/b978-0-12-816505-8.00007-2.
[66] S. Adhikari, S. Mandal, D. Sarkar, D.-H. Kim, G. Madras, Appl. Surf. Sci. 420 (2017) 472–482, https://doi.org/10.1016/j.apsusc.2017.05.191.
[67] Y. Xiao, J. Azaiez, J.M. Hill, Ind. Eng. Chem. Res. 57 (2018) 2705–2709, https://doi.org/10.1021/acs.iecr.7b04724.